PAPER • OPEN ACCESS

Concentric double hollow grid cathode discharges. Spectral investigations and phenomenological approach

To cite this article: C T Konrad-Soare et al 2021 Plasma Sources Sci. Technol. 30 085006

View the article online for updates and enhancements.

Concentric double hollow grid cathode discharges. Spectral investigations and phenomenological approach

C T Konrad-Soare[1,2,*] , F Enescu[1,2] , D G Dimitriu[2] , M Dobromir[3],
E G Teodorescu-Soare[4] , F Mazzanti[5], S A Irimiciuc[6] , C Ionita[1] and
R Schrittwieser[1]

[1] Institute for Ion Physics and Applied Physics, University of Innsbruck, Technikerstr. 25, A-6020, Innsbruck, Austria
[2] Faculty of Physics, Alexandru Ioan Cuza University, Carol I Blvd. 11, 700506, Iasi, Romania
[3] Institute of Interdisciplinary Research, Department of Exact and Natural Sciences, Alexandru Ioan Cuza University of Iasi, 11 Carol I Blvd., 700506, Iasi, Romania
[4] Faculty of Agriculture, Ion Ionescu de la Brad University of Agricultural Sciences and Veterinary Medicine, M. Sadoveanu Alley 3, 700490, Iasi, Romania
[5] University College Dublin, 4 Stillorgan Road, Belfield, Dublin, Ireland
[6] National Institute for Laser, Plasma and Radiation Physics, 409 Atomistilor Str., Bucharest, Romania

E-mail: claudia.konradsoare@gmail.com

CrossMark

Abstract
A discharge plasma is created by simultaneously biasing two concentric spherical grids with axisymmetric orifices. In this geometry, space charge structures in the form of multiple quasi-spherical luminous plasma bodies appear simultaneously inside and around the cathodes. The plasma formations are highly interdependent supplying each other with the particle flow and current closure necessary for the maintenance of the discharge. To diagnose these structures, space-resolved cold Langmuir probe measurements and optical emission spectroscopy investigations were performed in the axial direction allowing for the mapping of the axial profiles of plasma potential, electron temperature and density, ion density and optical emission. The existence of an accelerating double layer in the vicinity of the holes has been confirmed here, and in previous research (Teodorescu-Soare C T *et al* 2016 *Phys. Scr.* **91** 034002; Schrittwieser R W *et al* 2017 *Phys. Scr.* **92** 044001; Teodorescu-Soare C T *et al* 2019 *Int. J. Mass Spectrom.* **436** 83). Besides the assessment of the relationship between discharge conditions and plasma parameters in the novel cathode system, the importance of a multiple concentric cathode discharge configuration is revealed for deposition applications.

Keywords: semi-transparent cathode, hollow-cathode discharge, space charge structures, plasma bubble, plasma fireball, plasma double layer, thin film deposition

(Some figures may appear in colour only in the online journal)

1. Introduction

This study proposes a phenomenological approach for the understanding of a low-temperature plasma discharge in a concentric double spherical grid cathode configuration with axisymmetrically aligned orifices [1–3], and points out its importance for deposition applications. The basic understanding of transparent cathode discharges is relevant for basic plasma physics phenomena such as sheaths, electrostatic confinement, and particle thrusters. A number of basic aspects related to the discharge ignition by the simultaneous formation of interdependent plasma space charge structures (SCS) and the relationship between discharge conditions and plasma geometry are investigated.

In our case, a discharge plasma is created by negatively biasing the cathode arrangement with respect to the grounded chamber wall. Free electrons trapped within the negative confinement of the spherical grids are accelerated in a typical pendulum effect of a hollow cathode discharge (HC). With increasing applied negative bias on the grids, the electrons acquire sufficient energy to produce volume ionizations. In this geometry, complex SCS appear inside and around each grid once the elementary processes assure the necessary electric charge equilibrium [1, 2]. The extent of the spatial configurations varies with the applied cathode biases and background pressure [2]. To diagnose these structures, optical emission spectroscopy (OES) investigations and space-resolved cold Langmuir probe (CLP) measurements were performed in the axial direction, through the orifices of the cathode system. These measurements allowed for the axial mapping of the plasma potential, electron temperature and plasma density profiles, as well as describing the discharge geometry and the separate regions that appear in this particular kind of glow discharge. Maxima of the particle temperature and density have been recorded near the orifices due to local constrictions of the plasma potential in this region, as well as to the potential gradient of the double layer (DL) surrounding the fireball (FB)-like structure, which is reported here, and in previous research, in both single [1, 2] and double-grid configurations [3]. Luminous plasma structures in the form of quasi-spherical plasma bodies, called FBs or anode dots, frequently appear in plasmas attached to positively biased electrode surfaces [4–7]. In our case, the plasma FB evolves at the position of the orifices, inversely positioned, tangent to the spherical luminous interior with a streaming luminous tail towards the exterior as in the case of Hollow Cathode discharges.

HC-like designs are important in the construction of ion and Hall thrusters [8–11] and have been studied in recent years for geometry to power scaling [12–14]. As deposition sources they present a significant advantage to other well-established sputtering systems such as the magnetron [15, 16], allowing also for sputtering of ferromagnetic materials [17–19].

2. Methods and materials

The experiments were carried out in a grounded, stainless steel cylindrical chamber of 30 cm length and 18 cm diameter. Two concentric spherical grid electrodes of $d_i = 40$ mm inner and $d_e = 65$ mm outer grid diameters, with axisymmetrical orifices of $d_O = 0,5$ cm diameter each, 1 mm mesh width and 0,25 mm wire diameter, were simultaneously ignited in an Ar atmosphere at $p = 0,12$ mbar pressure.

The two spherical grid cathodes were negatively biased by using two *TDK-Lambda GENH600* power supplies in order to obtain the characteristic plasma formations for this specific type of discharge (see figure 1).

Detailed investigations of the SCS were carried out by optical and electrical means, in several discharge voltage scenarios, where different bias values were applied on the inner and outer grids, V_{int} and V_{ext}, respectively.

OES is a method used to extract plasma parameters of electrons involved in excitation collisions with neutrals such as the electron temperature, T_e^{exc} and the electron density, n_e^{exc} in local thermodynamic equilibrium conditions. The average T_e^{exc} was calculated by the line-to-line method [2] from the slope of the Boltzmann plot (where the intensity, I ratio of several spectral lines were plotted as a function of energy value, E_k). The density of electrons involved in excitation processes was calculated by using the relative intensities of $\lambda = 751,44$ nm neutral atomic Ar line and $\lambda = 476,48$ nm singly charged ionic Ar line according to the Saha–Egger equation. In our case, an *Ocean Optics HR4000* spectrometer was used to record the optic emission spectra of the plasma. The optical emission from portions of the plasma volume were focused by using an optical lens onto a parallel plane and collected with an optic fiber along the axisymmetrical *x*-coordinate.

Current–voltage (*I–V*) sweeps along the *x*-axis, starting from within the inner grid, $x = -10$ mm, through the two orifices and along the plasma elongation on the outside of the two cathodes were recorded by using a *Keithley 2611A* sourcemeter. The space resolved measurements were taken with a cylindrical CLP consisting of a 0,125 mm thick Tungsten wire with 1 mm of the metal exposed to the plasma. The tip of the probe was kept as small as possible in order to minimize the perturbation of the plasma structures known to be highly sensitive to the insertion of objects [20], but with sufficiently large surface area to collect detectable fluxes of charge carriers. These one-dimensional measurements allowed for mapping of the axial profiles of the plasma potential, Φ_P, the electron temperature, T_e and the plasma density, n_e.

In the second part of the experiments, the double-grid cathode configuration was investigated as a sputtering source. Four layers were deposited onto glass substrates in optimal deposition conditions described in section 3.3.

Optical transmittance spectra of the as-obtained thin films were recorded by using an *Evolution 300 UV–Vis Thermo Scientific* spectrophotometer in order to assort the layer opacity with the expected amount of deposited material. The chemical and elemental composition of the layers was derived from x-ray photoelectron spectroscopy (XPS) measurements performed with a *Physical Electronics PHI5000 VersaProbe* instrument. Prior to XPS measurements, the surfaces of the samples were subjected to Ar^+ bombardment (500 eV, 5 μA, 3 min) to remove the first atomic contaminant layer (in particular adventitious Carbon).
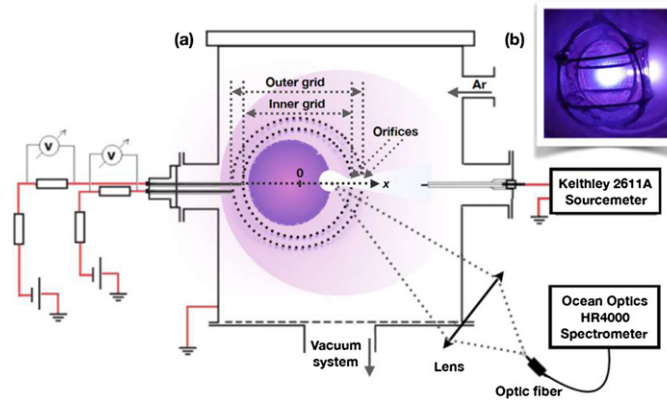
Figure 1. (a) Schematic representation of the double grid cathode configuration in the working regime, (b) photo of the discharge at $V_{\text{int}} = $ -300 V, $V_{\text{ext}} = 0$ V, $p = 0,12$ mbar, with $x = 0$ mm indicating the center of the grids.

3. Results and discussions

The primary region of the discharge is a uniform plasma situated in the centre of the inner sphere. The luminous core is surrounded by the cathode region where a significant potential drop between the grid and the plasma exists. Such structures are known in literature under the name of plasma bubbles (PB) [20–23]. Charge sheaths form on both inner and outer sides of the grid to shield the plasma from the negatively biased wires [21]. Due to the presence of the two axisymmetrically aligned orifices in the grids, a perturbation in the electric field appears, causing a slightly more positive potential region, which determines electrons from the PB to be accelerated toward its position. With increasing voltage (in absolute value) on the inner grid $|V_{\text{int}}|$, the thermal energy of the electrons from within the PB intensifies. Once the Debye length, $\lambda_{\text{D}} \sim \sqrt{T_{\text{e}}/n_{\text{e}}}$, of high-energy electrons drops below the orifices' diameter, they acquire sufficient thermal energy to escape the confinement of the negatively biased grid. This causes the appearance of a plasma DL with a low potential side tangent to the PB and a high potential side facing toward the exterior of the inner grid, resulting in charge separation at the orifice position. Under these conditions, an adjacent FB-like structure forms, attached to the PB's exterior. The semi-spherical DL exterior of the FB further accelerates the run-away electrons, which escape through its high potential side. Owing to this fact, a divergent electron beam can be observed emerging from the inner cathode sphere (see figure 1(b)). Aside from the relationship between discharge conditions, plasma geometry and sheath formation, the importance of a multiple concentric cathode discharge configuration is pointed out for deposition applications.

Plasma diagnostics through OES and CLP measurements were performed in order to follow the geometrical modifications of the SCS (such as their spatial extension on the *x*-axis) and the plasma parameter profiles evolution for several applied voltage scenarios on the two grids.

3.1. Discharge geometry

In order to better observe the discharge geometry, the axial distributions of the emission intensities I of $\lambda = 751,38$ nm emission line corresponding to excited (Ar*) atom and $\lambda = 476,48$ nm emission line to (Ar$^+$) ion along the symmetry *x*-axis are presented in figure 2. The vertical dashed lines represent the position of the two grids, while the arrow indicates the onset, equivalent to the DL position and the direction of the electron beam elongation. All measurements were taken along the symmetry axis of the discharge within the same spatial range with a common zero reference, $x = 0$ mm, at the center position of the concentric cathode arrangement, analog to the one indicated in figure 1(a). Though the intensities are presented in arbitrary units, their difference in magnitude is indicated on the *I*-axis.

A first set of measurements (A), was recorded for increasing negative bias applied on the inner grid, $V_{\text{int}} = -300$ to -500 V, with a voltage step, $V_{\text{step}} = -50$ V, while the outer grid was grounded, $V_{\text{ext}} = 0$ V. A significant luminosity increase of the discharge can be observed between these values (figures 2(a) and (b)). The discharge is limited, in this case, by the edge of the grounded outer grid $x = 33$ cm, where faint light emission can be seen in the immediate proximity of the outer grid and no emission is recorded on its outside beyond $x = 35$ mm as observed from the I profile variations. The second voltage configuration (B), consists of equal applied voltages on both grids, $V = V_{\text{ext}} = V_{\text{int}}$, taken between, $V = -300$ to -500 V, with a potential step, $V_{\text{step}} = -50$ V, to maintain comparability with set (A). The polarization of the outer grid significantly affects the spatial distribution of the discharge. The PB expands within the inner grid limit with increasing negative bias, while the electron beam lengthens beyond the outer grid edge up to $x = 70$ mm (figures 2(c) and (d)). Several common observations can be made for all discharge configurations. The light emission from both excited atoms and ions is faint and approximately constant on the exterior of the inner grid on the opposite side of the orifices, $x = -40$ to -20 mm. Once the inner grid edge is reached, the I values for both species increase monotonically, due to the presence of the PB in this region. The optical emission from both excited and ion species are at a plateau maximum that decreases abruptly in the second half of the inner sphere, $x = 0$–3 mm for configuration (A) and $x = 10$–15 mm for configuration (B). Due to the presence of the orifice, the PB is asymmetric on the *x*-axis. The
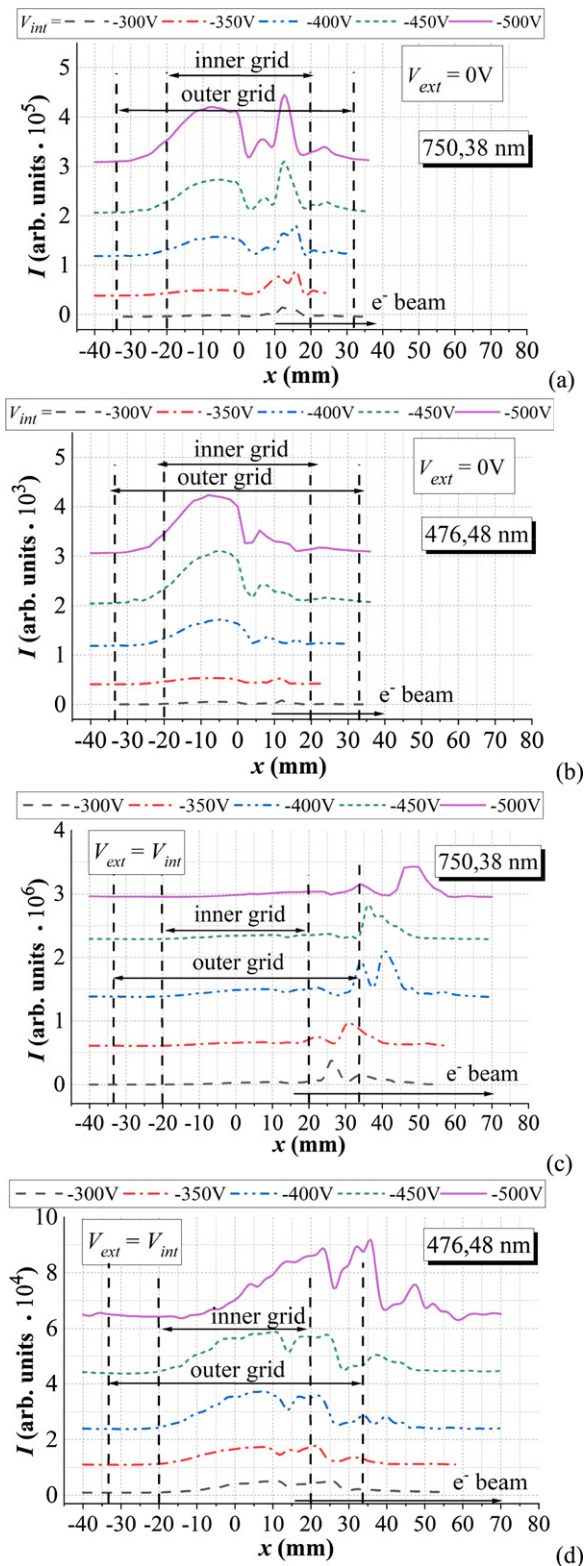
Figure 2. Axial distribution of optical emission intensity of Ar neutrals ($\lambda = 751.44$ nm) and Ar ions ($\lambda = 476.48$ nm) at $p = 0.12$ mbar for the discharge configurations A (a) and (b) and B (c) and (d).

following region is that of the DL. The initial emission peak corresponds to the maximum of the excitation cross section at the low potential side, followed by the high potential side equivalently to the onset of the streaming electron beam, where

high energetic electrons escape from the PB inner grid confinement. Within the latter structure the I drops down to a local minimum after which it increases again to a maximum value and then stabilizes. The peaks, noticeable on the exterior of the inner grid, indicate excitations and ionizations that occur within the electron beam's trajectory. The overall light emission increases with the applied voltage on the inner cathode V_{int}. This is an aspect seen throughout the entire inner sphere, due to increasing excitation and ionization rates that determine a higher emission. The intensity of the optical emission grows by approximately 6 times from $V_{\text{int}} = -300$ V to -500 V for case (A) (figures 2(a) and (b)). Though significant variations exist in the luminosity of the SCS for different V_{int}, the positions of the emission maxima and minima remain fairly constant, the structures' expansion being spatially restricted by the grounded outer grid. In the second bias configuration (B), by applying equal bias values on both grids, $V = V_{\text{int}} = V_{\text{ext}}$, a pronounced increase in luminosity is registered compared with case (A). The shapes of the axial distributions are similar to the ones presented previously, but unlike this situation, the peak intensities remain approximately equal, the emission intensity rising only by 50% from $V = -300$ V to -500 V. The noticeable difference appears in the spatial extent of the discharges beyond the outer grid, which in this case provides further acceleration for the run-away electrons. With increasing negative bias, the positions of the emission maxima and minima correlated to the maxima of the excitation and ionization cross sections, respectively, move progressively further away from the grids (figures 2(c) and (d)). Also, in comparison to configuration (A), the highest emission no longer comes from the PB within the inner grid, but from the exterior of the grids, where the run-away electrons collide with neutrals.

Concerning the emission ratio between the excited and ionized species, in both configurations (A) and (B), the ion emission is approximately 2 orders of magnitude lower than the excited atom emission, indicating a lower presence of the positive charge carriers along the symmetry x-axis. The presence of ions is mostly evident inside the PB, while on the exterior of the grids, only faint light emission of $\lambda = 476.48$ nm is recorded. This is due to the sum of contribution between ionizations caused by collisions between high-energetic electrons from the beam and neutrals and ion diffusion from the PB.

3.2. Plasma parameters

The previous observations are supported by the axial distribution profiles of the electron excitation temperature and density extracted from spectral measurements (figure 3).

OES is used in order to determine and prove the importance of excitation processes within the SCS. Both parameters maintain plateau values inside the PB, result consistent with the literature [20–23], followed by a peak increase at the low-potential side of the DL where the excitation cross section is at a local maximum. While in configuration (A) the DL is situated between, $x = 10$–20 mm (figures 3(a) and (b)), in configuration (B) a significant shift in its position occurs towards the right-hand side of the discharge between, $x = 20$–30 mm (figures 3(c) and (d)). The decrease in value of both $T_{\text{e}}^{\text{exc}}$ and $n_{\text{e}}^{\text{exc}}$ appears in the proximity of the grids, due to the energy
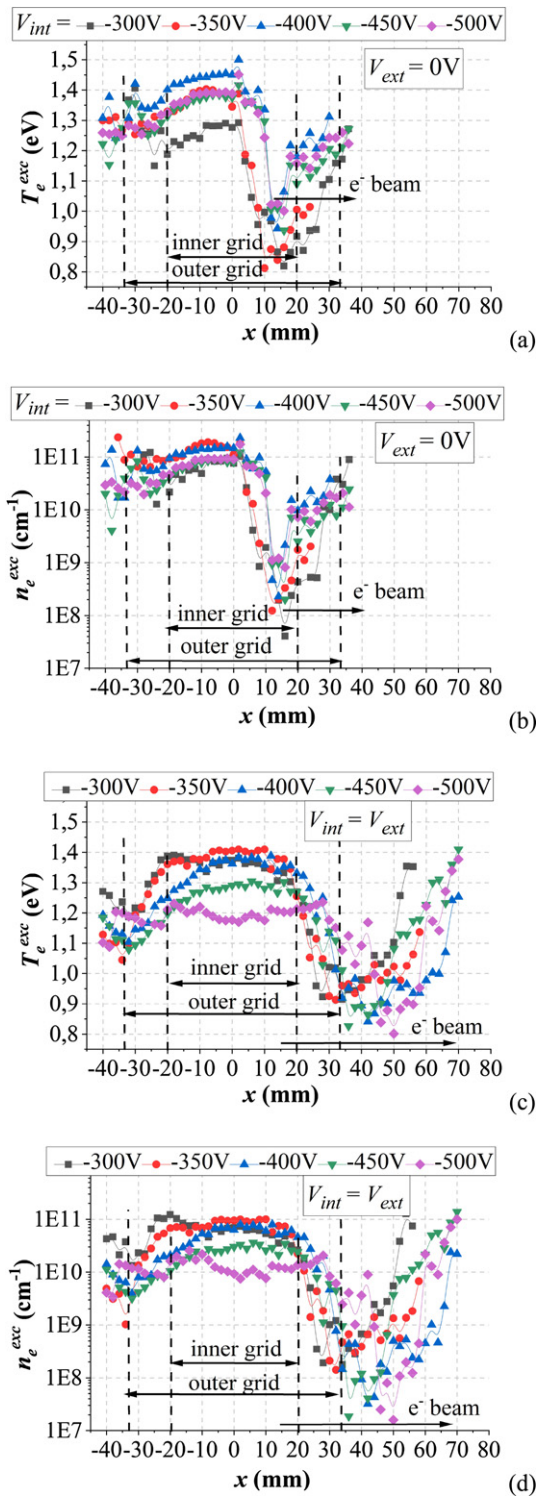
Figure 3. Plasma parameters extracted from OES measurements for the discharge configurations A (a) and (b) and B (c) and (d).

drop specific to a negative sheath. Also, the reduction of the electron density is characteristic to the low ionization rates in these areas (figures 3(b) and (d)). The further increase in values, noticeable from the trends of the T_e^{exc} and n_e^{exc} appearing after the DL positions, $x = 20–30$ mm (configuration (A)) and $x = 40–60$ mm (configuration (B)), are caused by inelastic collisions between neutrals and run-away electrons within the electron beam trajectory. The presence of these additional

charged particles on the exterior of the grids is essential for the preservation of the PB, which is highly dependant on particle exchange with the exterior plasma [20–23].

Electric diagnosis of the plasma structures was carried out in a complementary manner to the OES results. Space-resolved CLP measurements were performed in the axial direction through the orifices. Because of the sensitive nature of the discharge and the perturbance introduced by the CLP, only half of the inner grid area was successfully swept. Measurements were performed for configuration (B), due to better stability of the discharge that allowed for the axial scan from the inner grid centre through the orifices up to the exterior of the outer grid. Recordings of the axial profiles of the plasma parameters are presented in figure 4. Special emphasis has been given to the SCS region, $x = -10–40$ mm. Several common observations are valid. The plasma potential, Φ_P shows two plateau values with a steep potential jump, $V_{DL} \cong 15{,}6$ V related to the DL (figure 4(a)). This crucial difference is equal to the ionization potential of Ar. Concerning the electron temperature and particle densities, the distributions show a maximum at the position of the high potential side of the DL ($x = 20–25$ mm) where the ionization cross section is at a maximum value.

In our case, no background plasma is used. The primary discharge is ignited between the interior grid and the chamber walls [3]. Because the enclosing grid is negatively biased, free electrons are accelerated in a typical HC pendulum effect [17, 18], until they acquire sufficient energy to produce volume ionization within the inner grid volume [17]. Ions that result from the inelastic collisions diffuse at the Bohm velocity and are accelerated towards the grid wires. The mesh hole diameters, $d_m \approx 1$ mm do not allow for the escape of low-energy electrons, which are reflected and further accelerated in the pendulum effect. Once they reach sufficient thermal energies to overcome the potential barrier at the position of the largest orifice or when their Debye length becomes smaller than the orifice's diameter, $\lambda_D < d_O$, the electrons escape the inner grid confinement.

The presence of the orifice creates a discontinuity in the surrounding grid bias. The slightly more positive potential at this point is felt by the confined electrons, which are accelerated in the potential gradient. A well-defined luminous plasma DL is formed.

Once the potential drop across the DL is equal to the first ionization potential of the working gas, the necessary conditions for the formation of an FB are obtained. Because of its structural similarities to a classic plasma FB structure [6, 24, 25], we will refer to it as such. The FB has the shape of a drop inside the grid and the form of a streaming electron beam outside. The confined electrons of the PB are accelerated and can escape through the high potential side of the FB's DL, producing further excitations and ionizations on the outside of the grid (see figure 4(b)). Due to volume ionization, electron-ion pairs are formed outside the enclosing volumes of the inner cathode. A plasma cloud surrounds the cathodes mimicking an ambient plasma and supplies particles, which further sustain the PB [25, 26]. Because the electrons are accelerated towards the orifices, a strong presence is measured along the symmetry axis (figure 4(c)). On the other hand ions formed inside the PB
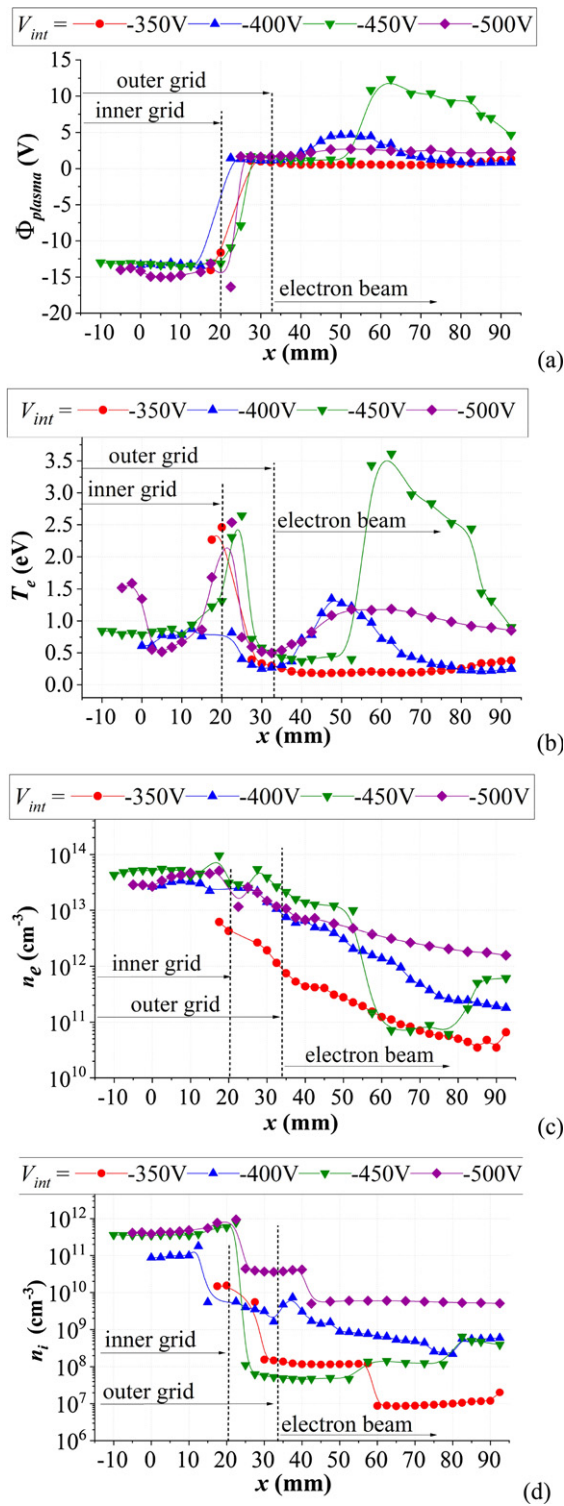
Figure 4. Axial distributions of (a) plasma potential, (b) electron temperature, (c) electron density and (d) ion density derived from CLP measurements.

Figure 5. Transmittance spectra recorded for the samples.
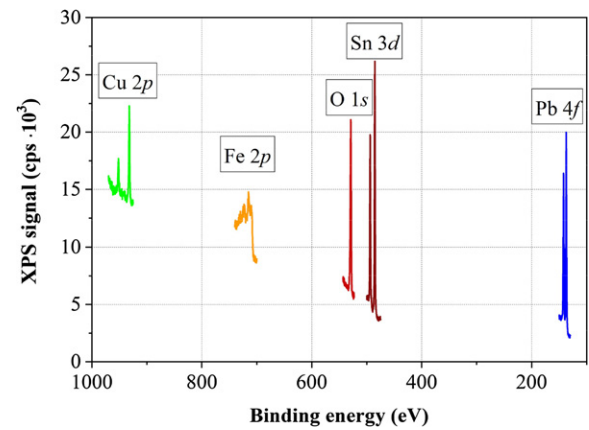
Figure 6. High-resolution XPS core level spectra of layer 4.

are rapidly accelerated towards the strongly negative cathode wires, their radial motion possibly explaining the lower values of the ion density along the measured *x*-axis (figure 4(d)).

Concerning the electron beam, the electron mean free path is approx. 1 mm for elastic collisions, meaning that most of the electrons are initially scattered through elastic collisions and explaining the 'cone shape' of the structure. Only high
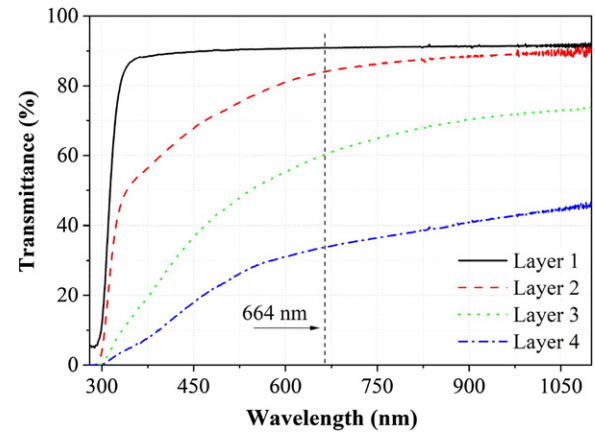
energetic tail electrons travel further outside the exterior of the grids. The increasing slope of the Φ_P (especially evident for $V = -350$ V), also contributes to the acceleration of the high-energetic run-away electrons.

The acceleration of the negative particles towards the DL causes a deficit of electrons in the PB and a voltage increase in the FB, enlarging the potential drop, V_{DL} [4, 27]. Because of the density reduction strong displacement currents appear in order to maintain charge neutrality [1, 2]. The DL surrounding the plasma FB expands and moves further inside the cathode, up to a certain distance where the current closure inside the PB can no longer be accounted for, collapsing into an electron-rich sheath [5], freeing the trapped particles that compensate then the particle deficit created in the PB. Because of the weakening of the DL in this stage, electrons are no longer sufficiently energetic that the electron λ_D is maintained lower than the grid's orifice diameter. The overall plasma potential of the structure is modified due to the DL disappearance [28]. The overall plasma density becomes lower with the collapse of the FB, allowing the electron sheath to expand again and a new DL to form [29].

Strong oscillatory phenomena are observed when the discharge voltage is reduced, along with flickering of the DL's luminous shell (results are presented in [1–3]). This phenomenon explains the results obtained in a previous work where instability modulation between the two plasma structures was observed [2].
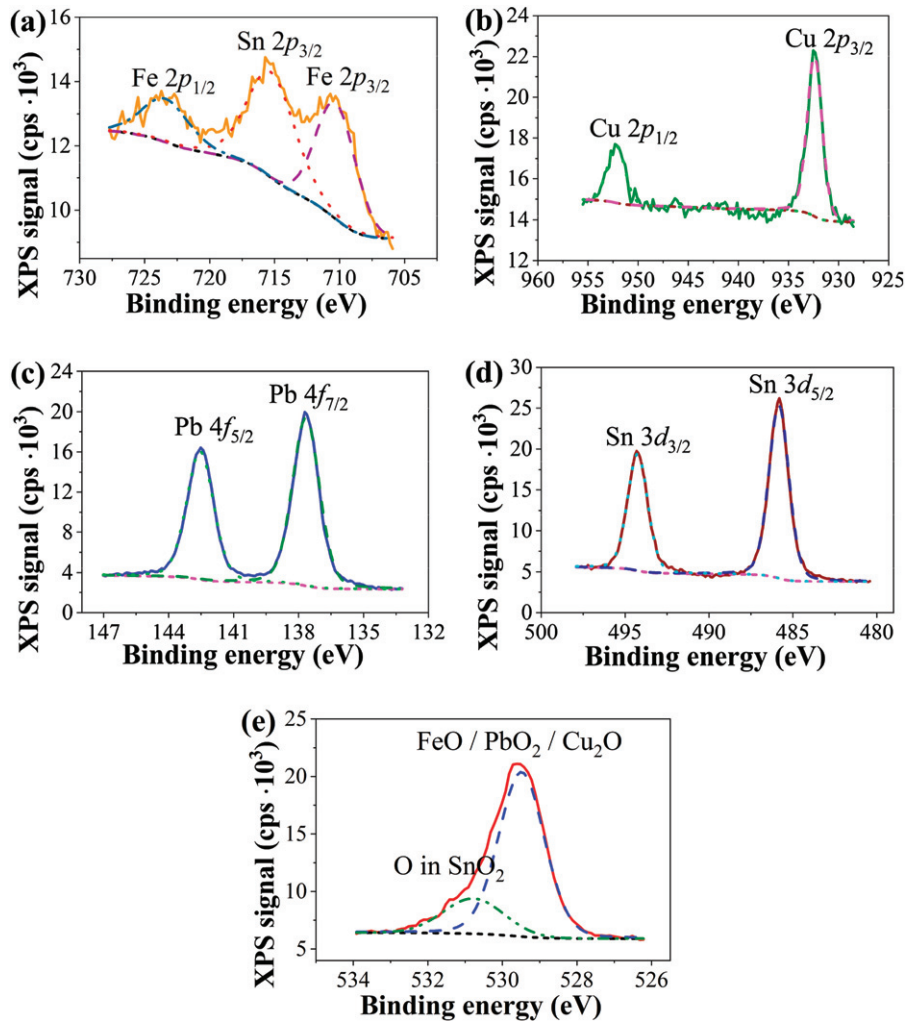
Figure 7. Deconvolution of high-resolution XPS spectra of layer 4 (a) Fe 2*p*, Sn 2*p* (b) Cu 2*p* (c) Pb 4*f* (d) Sn 3*d*5 and (e) O 1*s*.

3.3. Technical applications

Deposition applications of thin films in a HC discharge configuration are well established and have been used by several research groups [18, 19]. In this section, the possible use of the transparent double grid cathode discharge with axisymmetrically aligned orifices is investigated for sputtering and deposition applications. Similar to the HC discharge, material from the cathode is sputtered by heavy ion bombardment. In our case, Ar ions, initially produced within the PB, are radially accelerated towards the strongly negative metallic wires causing the grid material to be sputtered. Because the cathode is in this case also the target, the range of deposition materials is limited to electric conductors.

Glass substrates have been placed in front of the outer grid at a distance, $d = 15$ mm, in the electron beam's path. Depositions have been made in the bias configuration (B) for times of $t = 90$ min each. Both applied voltages were increased concomitantly in absolute value between $V = -350$ to -500 V, with a voltage step of $V_{step} = -50$ V at a pressure of $p = 0,12$ mbar. These optimal values have been chosen to obtain the highest cathode sputtering rate within the given device limitations.

Optic transmittance spectroscopy measurements were performed on the depositions. Higher applied negative grid discharge biases are associated with higher sputtering rates and consequently related to higher amounts of deposited material. The transparency of the deposited layers was derived for wavelengths between 300–1050 nm (figure 5). Considering $\lambda = 664$ nm (blue wavelength) as an example, layer 1, obtained for $V = -350$ V has a transparency T of 90,9%, while for the following layers it registers a consistent decrease: layer 2, $T = 83,9\%$ ($V = -400$ V), layer 3, $T = 60,3\%$ ($V = -450$ V) and layer 4, $T = 33,8\%$ ($V = -500$ V).

High resolution XPS was used to determine the elemental and chemical composition of the layers deposited under the above-mentioned conditions. The spectra revealed similar concentrations in all the investigated samples. Specifically, only the results for layer 4 will be presented here as an example. The following signals were recorded: Fe 2*p* in proportion of 29,5%, Cu 2*p* - 10,7%, Pb 4*f* - 9,0% and Sn 3*d* - 6,5% along with O 1*s* in high amounts corresponding to the oxides of the metals (figure 6).

The deconvolution of the high-resolution XPS spectra recorded for layer 4 is depicted in figure 7. Iron is the

main component of the metallic mesh wire, appearing in the high-resolution XPS spectra as a convolution of two neighbouring peaks, Fe $2p$ 3/2 at the binding energy (BE) = 710,3 eV in FeO bond [30] and Fe $2p$ 1/2 at BE = 723,2 eV corresponding to FeO bond [31]. Iron oxides have a significant shift to higher values of the BE than that of metallic Fe at BE = 706,7 eV [31]. The next highest concentration element is Copper, Cu $2p$ found at BE = 952,5 eV - Cu $2p$ 1/2 [32] and BE = 932,7 eV—Cu $2p$ 3/2 [33] both corresponding to the Cu_2O bond. The Cu $2p$ peak has significant split spin–orbit components of approx. 19,75 eV. Other metals such as Lead–Pb $4f$ and Tin–Sn $3d$ are present on the glass surfaces. Pb $4f$ is present in lead dioxide (PbO_2) form at BE = 141,7 eV - Pb $4f$ 5/2 [34] and at BE = 137,6 eV - Pb $4f$ 7/2 [35], respectively, having well separated orbit components. Tin (II) oxide – Sn $3d$ 3/2 at BE = 494,5 eV [36] and Tin (IV) dioxide – Sn $3d$ 5/2 at BE = 486,6 eV [37] exists along with Sn $3p$ 3/2 at BE = 716,0 eV – Tin (IV) dioxide, corresponding to SnO_2 molecule [38].

The presence of Oxygen in such a high amount at BE = 529,2 eV and BE = 530,9 eV suggests that the O $1s$ peaks are due to the sum of contributions of all metal-oxide bonds: PbO_2 at BE = 528,8 eV [35], FeO at BE = 529,5 eV [30], Cu_2O at BE = 530,7 eV [39] and SnO_2 at BE = 530,9 eV [40].

The presence of a mixture of oxide bonds from several elements in the thin films compositions indicates the possibility of obtaining different surface reactivity by customizing their ratio. Modifying the flow of Oxygen and thus its availability during layer growth can influence the stoichiometry of the layers and enhance the presence of suboxides, modifying the energy band configuration in such heterojunction materials [41, 42]. This aspect is directly related to the surface reactivity of semiconductor materials (e.g. photocatalysis, wettability).

4. Conclusions

Interdependent plasma SCS are formed in a double spherical grid cathode configuration with axisymmetrically aligned orifices. A PB is situated at the centre of the inner sphere, surrounded by the negatively biased inner-grid. Due to the presence of the orifices, a slightly more positive potential region appears, permitting high-energy electrons to escape the grid confinement, as long as their thermal energies are sufficiently high for their Debye length to fall below the orifice diameters. Owing to this fact, a plasma DL forms at this position allowing for an inversely-positioned plasma FB to appear, tangent to the PB with an emerging beam of electrons. The electron beam in turn determines further ionizations on the outside of the outer-grid, which enable the formation of a plasma cloud around the spheres. The ignition of the discharge is only made possible in the absence of background plasma due to the presence of the orifices, which allow for the three interdependent plasma structures to form and supply each other the necessary particle flow and current closure. The semi-transparent cathode discharge is highly dependent on the applied negative bias. Appropriate discharge conditions were obtained in order for thin films from the grid-cathode material to be deposited onto glass substrates.

These findings allow for the further understanding of semi-transparent cathode discharges and reveals their importance for particle confinement and deposition applications.

Data availability statement

The data that support the findings of this study are available upon reasonable request from the authors.

ORCID iDs

C T Konrad-Soare ⬤ https://orcid.org/0000-0003-3840-7933
F Enescu ⬤ https://orcid.org/0000-0002-2828-7053
D G Dimitriu ⬤ https://orcid.org/0000-0002-2474-5133
E G Teodorescu-Soare ⬤ https://orcid.org/0000-0003-4094-2222
S A Irimiciuc ⬤ https://orcid.org/0000-0002-4592-6814
C Ionita ⬤ https://orcid.org/0000-0003-4875-6213
R Schrittwieser ⬤ https://orcid.org/0000-0002-6403-0511

References

[1] Teodorescu-Soare C T, Dimitriu D G, Ionita C and Schrittwieser R W 2016 *Phys. Scr.* **91** 034002
[2] Schrittwieser R W, Ionita C, Teodorescu-Soare C T, Vasilovici O, Gurlui S, Irimiciuc S A and Dimitriu D G 2017 *Phys. Scr.* **92** 044001
[3] Teodorescu-Soare C T, Irimiciuc S A, Ionita C, Dimitriu D G, Hodoroaba B, O'Hara T, Vasilovici O, Amarandi L and Schrittwieser R W 2019 *Int. J. Mass Spectrom.* **436** 83
[4] Ionita C, Dimitriu D G and Schrittwieser R W 2004 *Int. J. Mass Spectrom.* **233** 343
[5] Stenzel R L, Ionita C and Schrittwieser R 2008 *Plasma Sources Sci. Technol.* **17** 035006
[6] Popescu S 2006 *Europhys. Lett.* **73** 190
[7] Baalrud S D, Scheiner B, Yee B T, Hopkins M M and Barnat E 2020 *Plasma Sources Sci. Technol.* **29** 053001
[8] Kanev S V, Khartov S A and Nigmatzyanov V V 2017 *Procedia Eng.* **185** 31
[9] Xia G, Liu X, Li H, Ding Y, Wei L, Chen S and Yu D 2020 *Vacuum* **172** 109052
[10] Kralkina E A, Vavilin K V, Zadiriev I I, Nekliudova P A and Shvydkiy G V 2019 *Vacuum* **167** 136
[11] Meng T, Qiao C, Wang Y, Ning Z and Yu D 2020 *Vacuum* **172** 109040
[12] Domonkos M T and Gallimore A D 1997 *25th Int. Electric Propulsion Conf. IEPC-97-189*
[13] Farnell C C, Williams J D and Wilbur P J 2003 *28th Int. Electric Propulsion Conf. IEPC-03-072*
[14] Pedrini D, Albertoni R, Paganucci F and Andrenucci M 2013 *33rd Int. Electric Propulsion Conf. IEPC-2013-111*
[15] Kelly P J and Arnell R D 2000 *Vacuum* **56** 159
[16] Manole V A, Dobromir M, Apetrei R, Nica V and Luca D 2014 *Ceram. Int.* **40** 9989

[17] Siegfried D E and Wilbur P J 1983 *AIAA J.* **21** 5
[18] Apetrei R, Alexandroaei D, Luca D, Balan P, Ionita C, Schrittwieser R and Popa G 2006 *Japan. J. Appl. Phys.* **45** 8128
[19] Schrittwieser R *et al* 2010 *J. Plasma Phys.* **76** 655
[20] Stenzel R L and Urrutia J M 2012 *Phys. Plasmas* **19** 082105
[21] Stenzel R L and Urrutia J M 2012 *Phys. Plasmas* **19** 082106
[22] Stenzel R L and Urrutia J M 2012 *Phys. Plasmas* **19** 082107
[23] Stenzel R L and Urrutia J M 2012 *Phys. Plasmas* **19** 082108
[24] Song B, D'Angelo N and Merlino R L 1991 *J. Phys. D: Appl. Phys.* **24** 1789
[25] Stenzel R L, Gruenwald J, Ionita C and Schrittwieser R 2011 *Plasma Sources Sci. Technol.* **20** 045017
[26] Agop M, Dimitriu D G, Niculescu O, Poll E and Radu V 2013 *Phys. Scr.* **87** 045501
[27] Dimitriu D G, Aflori M, Ivan L M, Ionita C and Schrittwieser R W 2007 *Plasma Phys. Control. Fusion* **49** 237
[28] Stenzel R L, Gruenwald J, Ionita C and Schrittwieser R 2012 *Plasma Sources Sci. Technol.* **21** 015012
[29] Oprescu B and Popescu S 2000 *J. Phys. D: Appl. Phys.* **33** 2284
[30] Allen G C, Curtis M T, Hooper A J and Tucker P M 1974 *J. Chem. Soc. Dalton Trans.* **14** 1525
[31] Wang Y, Wang L L and Sun C Q 2009 *Chem. Phys. Lett.* **480** 243
[32] Jolley J G, Geesey G G, Hankins M R, Wright R B and Wichlacz P L 1989 *Appl. Surf. Sci.* **37** 469
[33] Seah M P 1989 *Surf. Interface Anal.* **14** 488
[34] Rogers J D, Sundaram V S, Kleiman G G, Castro S G C, Douglas R A and Peterlevitz A C 1982 *J. Phys. F: Met. Phys.* **12** 2097
[35] Kanai H, Yoshiki M, Hayashi M, Kuwae R and Yamashita Y 1994 *J. Am. Ceram. Soc.* **77** 2229
[36] Shiratsuchi R, Hongo K, Nogami G and Ishimaru S 1992 *J. Electrochem. Soc.* **139** 2544
[37] Stranick M A and Moskwa A 1993 *Surf. Sci. Spectra* **2** 50
[38] Morgan W E and Van Wazer J R 1973 *J. Phys. Chem.* **77** 964
[39] Otamiri J C, Andersson A, Andersson S L T, Crow J E and Gao Y 1991 *J. Chem. Soc. Faraday Trans.* **87** 1265
[40] Di Giulio M, Serra A, Tepore A, Rella R, Siciliano P and Mirenghi L 1996 *Mater. Sci. Forum* **203** 143
[41] Teodorescu-Soare C T, Dobromir M, Ciobanu A, Luca M, Stoian G and Luca D 2019 *Semicond. Sci. Technol.* **34** 075027
[42] Dobromir M, Konrad-Soare C, Stoian G, Semchenko A, Kovalenko D and Luca D 2020 *Nanomaterials* **10** 1901